Constraining Sector-specific CO2 Fluxes using Space-based XCO2 Observations over the Los Angeles Basin

Dustin Roten[1], John C. Lin[2], and Eric A. Kort[3]

[1]Jet Propulsion Laboratory, California Institute of Technology
[2]University of Utah
[3]University of Michigan-Ann Arbor

May 4, 2023

Abstract

The concentration of carbon dioxide (CO2) in Earth's atmosphere is increasing due to human activities and the resulting effects on the global climate system have initiated sev- eral policy-driven approaches to reduce emissions of this greenhouse gas. Quantifying the effectiveness of such policies requires both bottom-up and top-down approaches to estimate CO2 emissions. This work investigates, for the first time, the potential of using SAM observations from NASA's OCO-3 instrument to disaggregate sector-specific emissions from instrument observations. Optimized sector-specific timeseries were produced using Bayesian inversion techniques and compared to proxy activity data from the transportation, commercial maritime, and industrial sectors. Results demonstrate that dense space-based observations of atmospheric CO2 are capable of disentangling sector-specific CO2 fluxes, paving the way for accurate monitoring of the effects of carbon-reduction policies and operational carbon monitoring systems.

Hosted file

`962184_0_supp_10947290_rtzm5s.docx` available at https://authorea.com/users/613971/articles/641068-constraining-sector-specific-co2-fluxes-using-space-based-xco2-observations-over-the-los-angeles-basin

Constraining Sector-specific CO_2 Fluxes using Space-based XCO_2 Observations over the Los Angeles Basin

Dustin Roten[1], John C. Lin[2], Eric A. Kort[3]

[1] Jet Propulsion Laboratory, California Institute of Technology, Pasadena, CA, USA
[2] Department of Atmospheric Sciences, University of Utah, Salt Lake City, UT, USA
[3] Climate and Space Sciences and Engineering, University of Michigan, Ann Arbor, MI, USA

Key Points:

- NASA's OCO-3 instrument provides the densest spatial coverage of urban XCO_2 from space, which includes information on spatially variant surface fluxes. We show this spatial coverage makes it possible to disaggregate sectoral emissions information from observations.
- Using OCO-3 and the Los Angeles Basin as a case study, three emission sectors from an emission inventory are optimized to include effects from COVID-19 lockdowns. In two contributing sectors, On-road Transportation and Industry, optimized CO_2 flux decreased considerably around the time COVID-19 lockdowns were implemented in the Los Angeles area. In the third sector, Maritime Transportation, optimized CO_2 flux steadily increased over time.
- The timeseries of optimized fluxes followed sector-specific proxy data.

Corresponding author: Dustin Roten, `droten@jpl.nasa.gov`

Abstract

The concentration of carbon dioxide (CO_2) in Earth's atmosphere is increasing due to human activities and the resulting effects on the global climate system have initiated several policy-driven approaches to reduce emissions of this greenhouse gas. Quantifying the effectiveness of such policies requires both bottom-up and top-down approaches to estimate CO_2 emissions. This work investigates, for the first time, the potential of using SAM observations from NASA's OCO-3 instrument to disaggregate sector-specific emissions from instrument observations. Optimized sector-specific timeseries were produced using Bayesian inversion techniques and compared to proxy activity data from the transportation, commercial maritime, and industrial sectors. Results demonstrate that dense space-based observations of atmospheric CO_2 are capable of disentangling sector-specific CO_2 fluxes, paving the way for accurate monitoring of the effects of carbon-reduction policies and operational carbon monitoring systems.

Plain Language Summary

Carbon dioxide (CO_2) is a key greenhouse gas and several local-to-international policies are in place to reduce the amount being emitted by human activities. This work investigates the amount of CO_2 emitted within the Los Angeles Basin during the period between January 2020 and December 2021 using NASA's Orbiting Carbon Observatory-3. The observed emissions are broken down into contributions from specific sectors (on-road transportation, industrial sources, commercial maritime activity, etc.) The results of this work demonstrate that urban CO_2 emissions observed from space-based instrumentation can be disaggregated to several socioeconomic sectors to study trends that may be present in each one. Notable detected features include the sudden reduction of on-road CO_2 emissions due to the COVID-19 lockdown period and the steady increase in off-shore emissions due to ship idling and delays. The effectiveness of current and future policies regarding sector-specific reductions have the potential to be observed over time using the framework presented here.

1 Introduction

Carbon dioxide from the combustion of fossil fuels ($FFCO_2$) is among the most important greenhouse gases in the atmosphere (Zhong & Haigh, 2013). Anthropogenic activities typically associated with cities are a significant source (Intergovernmental Panel on Climate Change, 2015). Efforts to constrain estimates of these emissions use two methods: "bottom-up" inventory estimates and "top-down" atmospheric observations. Bottom-up methods use a variety of activity data and statistical methods to construct approximate distributions of $FFCO_2$ fluxes across many geographic scales (Oda et al., 2018; Janssens-Maenhout et al., 2019; Gurney et al., 2020; Gilfillan & Marland, 2021). However, this reliance on multiple data streams often delays the release of updated inventories, as many sources have coarse temporal resolution and/or take time to update (Roten, Marland, et al., 2022). Furthermore, variations in construction methods create substantial differences between inventories (Hutchins et al., 2016). Some cities host ground-based (top-down) CO_2 observing networks that record atmospheric measurements at a high temporal resolution. While these observations provide a means to constrain the "true" magnitude of emissions from urban areas and validate inventories, these networks are limited to a handful of cities, have few instrument sites, and require sophisticated interpretation to disentangle urban signals (Bares et al., 2019; Lauvaux et al., 2016; Shusterman et al., 2016). Results from both methods are used to inform carbon cycle science and reduction policies at local, national, and international scales.

Space-based carbon-observing instruments are providing routine observations at near-global coverage with revisit times ranging from three to 16 days (Janssens-Maenhout et al., 2020). These increases in spatiotemporal coverage address the shortcomings of cur-

rent bottom-up and top-down methodologies. As observations are collected over time, spatial gradients and localized enhancements are revealed, driven by emissions from populated areas (Hakkarainen et al., 2016). Although the signals detected by space-based instruments are inherently attenuated due to column-averaging (Rayner & O'Brien, 2001; Keppel-Aleks et al., 2011), these observations are capable of providing insights into localized urban emissions. Many studies show that transects obtained by NASA's Orbiting Carbon Observatory-2 (OCO-2) near urban areas are useful in constraining local CO_2 emissions (Lu et al., 2018; Hedelius et al., 2018; Wu et al., 2018; Yang et al., 2020; Wu et al., 2020) even though the original intent of this instrument was to inform carbon cycle science at regional/global scale (Crisp et al., 2004).

The installation of OCO-3 on the International Space Station (ISS) in 2019 allows for the collection of spatially dense soundings over targeted urban areas. This new type of observation, referred to as "Snapshot Area Maps" (SAMs), covers a domain of roughly 80km × 80km with individual atmospheric soundings spaced roughly 2km apart (Eldering et al., 2019). This increased density allows sub-city spatial features to be resolved in XCO_2-space and provides more emission information than other space-based instruments (Kiel et al., 2021). Furthermore, the orbit of the ISS allows SAMs to be collected at varying daytime hours as opposed to the narrow time window (around 1:30pm local time) that previous instruments such as OCO-2 are restricted to (Crisp et al., 2004; Eldering et al., 2019). Using Bayesian inversion techniques (Rodgers, 2000), these sub-city enhancements can inform the construction of emission inventories that represent surface emissions in flux-space (Roten, Lin, et al., 2022) (referred to hereafter as RL22). RL22 provides a "first look" into the potential of using OCO-3 SAMs to optimize sector-specific urban flux estimates by constructing an observing system simulation experiment (OSSE). Their results suggest that individual SAMs provide minimal spatial optimization of prior inventories while aggregating SAMs over time generated useful scaling factors for sector-specific emission estimates.

Although Bayesian methods are frequently applied to ground-based CO_2 networks (Kunik et al., 2019; Mallia et al., 2020; Turner et al., 2020; Lauvaux et al., 2020), the number of applications using XCO_2 observations is growing (Ye et al., 2020; Shekhar et al., 2020). For instance, Ye et al. (2020) used OCO-2 observations over the Los Angeles Basin to calculate optimized scaling factors for emissions estimates provided by the ODIAC inventory (Oda et al., 2018) with factors ranging from 0.66 to 1.84. While previous studies focused on optimizing total emissions from a "whole-city" perspective, this work demonstrates the potential of disaggregating sector-specific contributions to CO_2 enhancements measured from a space-based instrument in near-real-time. Timeseries of optimized emissions from sector-specific sources were compared with hourly roadway traffic, monthly marine activity, and annual industry emission data and show good agreement with expected trends. Decreases in emissions during LA's COVID-19 lockdowns (Laughner et al., 2021) were also detected by OCO-3. Results demonstrate that space-based XCO_2 observations are capable of optimizing multiple emission sectors within the LA domain, highlighting the importance of regular high-resolution measurements for the purposes of constraining sector-specific emissions and quantifying the short-term effectiveness of sector-specific carbon reduction policies. Additionally, the techniques presented in this work show potential to be applied broadly to multiple cities around the world, providing a piece of the framework for a global near-real-time carbon monitoring system.

2 Methods

2.1 Study Domain: The Los Angeles Basin

The United States Census Bureau reports that the Los Angeles metro area is home to roughly 13 million people. This megacity sits along the southern California coast and

has two active maritime ports, multiple international airports, and several traversing interstate highways. This area hosts large coastal industrial complexes and sizable power plants to the south. The CO_2 emission domain considered in this work covers much of the Basin area, including the San Fernando and San Bernardino Valleys (see **Figure 1 (top)**). OCO-3 has collected more than 50 target and SAM observations over this area between 8:00am and 6:00pm local time. Each sounding making up these SAMs is treated as an independent observation of column-averaged CO_2 ($XCO_{2,obs}$) and is assumed to be the summation of three components:

$$XCO_{2,obs} = XCO_{2,urban} + XCO_{2,bkg} + XCO_{2,bio:urban}. \tag{1}$$

$XCO_{2,urban}$ is the fossil contribution from the urban domain of interest, $XCO_{2,bkg}$ is the contribution from residual sources (anthropogenic and biospheric) outside of the domain, and $XCO_{2,bio:urban}$ is the biospheric impact on $XCO_{2,urban}$. Isolating $XCO_{2,urban}$ of each sounding and comparing it to modeled estimates provides the constraint on the emission estimate. Additionally, $XCO_{2,bkg}$ can be further broken down into two terms:

$$XCO_{2,bkg} = XCO_{2,bkg:bio} + XCO_{2,bkg:other}. \tag{2}$$

Here, $XCO_{2,bkg:bio}$ represents the influence that the biosphere has on the background estimation and $XCO_{2,bkg:other}$ represents the remainder.

Surface CO_2 flux from the domain was represented by the Vulcan 3.0 emission inventory (Gurney et al., 2020) using the latest available year (2015). This spatially explicit emission inventory contains 10 sectors that span residential, commercial, and industrial sources at a 1km $\times$ 1km resolution. The on-road transportation sector is responsible for almost half (42%) of the urban emissions from LA followed by the industrial (26%). A weaker yet important source is the commercial maritime sector (2%), which is confined along the coast of the LA and is not coincident with other significant emission sectors. The spatial distribution of the on-road, industrial, and marine sectors are included in **Figure 1 (bottom)**. (Spatial plots of emissions from other sectors are included in the **Supporting Information**.)

Individual XCO_2 soundings are irregularly gridded across the domain and are affected by clouds, aerosols, and viewing geometry (Eldering et al., 2019). Using the column-averaged Stochastic Time-Inverted Lagrangian Transport (X-STILT) model (Wu et al., 2018), an influence footprint was generated for each good quality sounding across all SAMs (see RL22 for further information regarding the setup of this model for LA). These X-STILT footprints were convolved with the Vulcan 3.0 emission inventory to calculate modeled $XCO_{2,urban}$ values at each sounding location. Soundings where the contribution from LA was ≤ 0.01ppm, as calculated by X-STILT, identified "background" soundings for each SAM. The average of these soundings was used as $XCO_{2,bkg}$. Biospheric influences, making up ∼20% of the variability in the LA region (Miller et al., 2020), were incorporated with the Solar-Induced Fluorescence for Modeling Urban Biogenic Fluxes (SMUrF) model (Wu et al., 2021). Using observations of solar-induced fluorescence from space, SMUrF generates a spatially explicit inventory of the hourly net ecosystem exchange of CO_2. Footprints were convolved with SMUrF output to remove per sounding biospheric influences ($XCO_{2,bio:urban}$ and $XCO_{2,bio:bkg}$).

2.2 Proxy Data and Uncertainty

Although estimated CO_2 flux is provided at an hourly timescale, the Vulcan 3.0 emission inventory only provides spatially explicit high and low estimates (uncertainties) of these fluxes at an annual scale (Gurney et al., 2020). For each cell, the maximum of
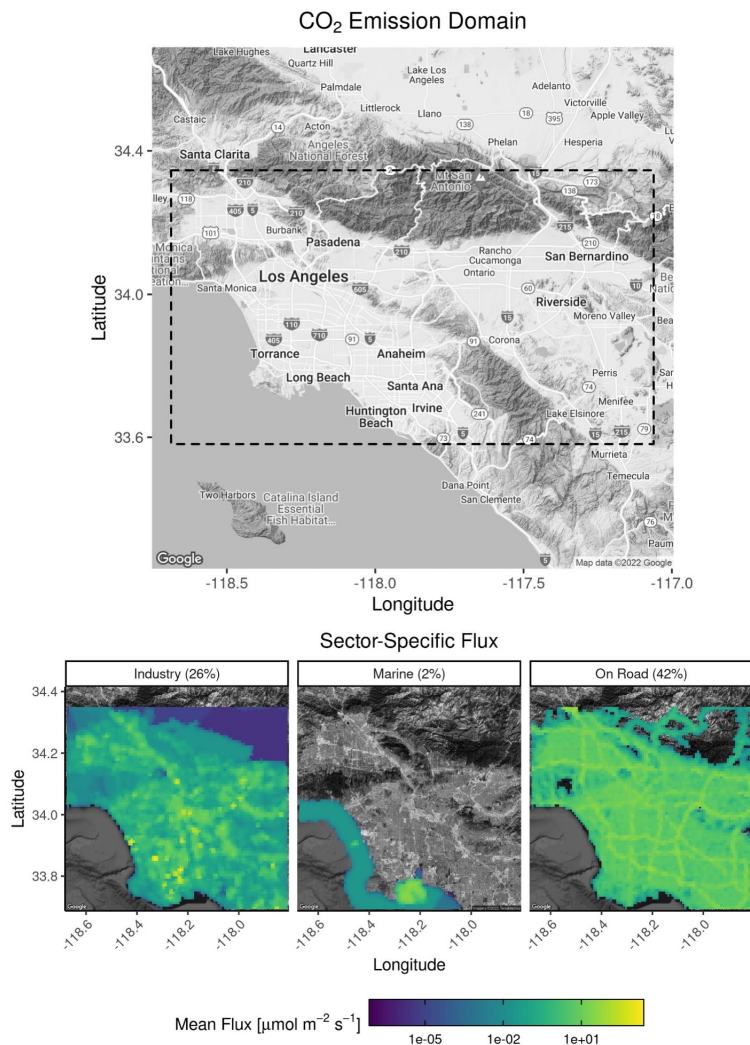
Figure 1. A description of the domain of interest. The urban domain includes the Los Angeles Basin, San Fernando Valley, and San Bernardino Valley (black rectangle, top). The spatial distribution of selected sectoral emissions from Vulcan 3.0 are presented in the bottom panels (emission estimates are from year 2015).

the absolute differences between these high/low estimates was used to assign an uncertainty estimate. The sum of these per-cell values provided an overall uncertainty estimate for each sector. While this methodology reflected typical uncertainty values, changes in socioeconomic dynamics due to the COVID-19 pandemic influenced CO_2 fluxes considerably (Laughner et al., 2021). The initial uncertainties derived from annual Vulcan 3.0 estimates are averaged from a typical year of emissions. No sudden socioeconomic changes were present in these estimates, suggesting that they were underestimates when applied to the 2020/2021 time frame. To address this shortcoming, independent sources of activity data were used to calculate alternative uncertainty values for several sectors. These values specifically incorporated socioeconomic fluctuations from the COVID-19 pandemic and replaced previously calculated uncertainty estimates when possible. Descriptions of the available activity data relevant to the on-road, industrial, and marine

sectors are presented below and summarized in **Table 1**. (Discussion of proxy data beyond the primary sectors featured here are included in the **Supporting Information**.)

2.2.1 On-road Transportation

There are efforts to record trends in several economic sectors in LA. A notable example is the California Department of Transportation's Performance Measurement System (PeMS) which uses an array of sensors to collect traffic data from the interstate highways throughout the state. In this work, data from five highways traversing the basin (10, 105, 210, 405, 605) were aggregated to produce daily total traffic counts for years 2015, 2020, and 2021. These values were then multiplied by average annual per-mile CO_2 emissions factors from the EPA (EPA, 2021). The daily percent change from 2015 was calculated by comparing each day of the 2020/2021 time period to its corresponding day in 2015. Comparing weekdays and weekend days to corresponding days in 2015 eliminated weekday/weekend mismatch. The maximum change in on-road activity during the 2020/2021 time period occurred during March 2020 with a reduction of roughly 50%.

2.2.2 Industry

The U.S. Environmental Protection Agency (US EPA) provides annual datasets for large point source emitters. The dataset used in this work is from the Greenhouse Gases Reporting Program (GHGRP). It includes voluntarily reported CO_2 emissions from point sources beyond power generation facilities (such as large industrial manufacturers). Due to the voluntary nature of GHGRP reporting, point sources reported in 2015 are not guaranteed to be included in 2020/2021. Comparing annual totals between 2015 and 2020 revealed a 60% reduction from these point sources. In an alternative calculation, using only point sources present in both datasets, GHGRP revealed a reduction of 12%. Using annual totals, Vulcan 3.0 provides a maximum difference of 38%. This intermediate value was used as the uncertainty for the industrial sector.

2.2.3 Marine

The Ports of Los Angeles and Long Beach maintain monthly records of port activity through container movement. Monthly trends in passenger and cargo totals in 2020/2021 were compared to base values from 2015. During the span of 2020, a steady increase in passenger and cargo activity at both ports is evident.

2.3 Errors in XCO$_2$-space

The Bayesian inversion scheme requires uncertainties in both prior fluxes and observations. Both of which are used in the construction of posterior scaling factors for each sector. Mismatches in modeled and observed XCO_2 values stem from the stochastic nature of the X-STILT model, improper characterization of the boundary layer height, errors in the horizontal wind speed/direction, instrument limitations, and uncertainty from the biospheric model. Wu et al. (2018) quantified transport uncertainties in the X-STILT model using global, low-resolution meteorological data while the meteorological fields used in this study were provided by the 3km High Resolution Rapid Refresh (HRRR) dataset (Benjamin et al., 2016). The uncertainties from the lower resolution meteorological fields from Wu et al. (2018) are included in **Table 2** and are assumed to be overestimates of HRRR uncertainties. Additionally, multiple studies have characterized OCO-3's retrieval error at both the local (LA) and global levels (Kiel et al., 2021; Taylor et al., 2020) where values range from 0.23 to 2ppm. A mid-range value of 1ppm was selected to represent the instrument error over LA area. Uncertainty in the net ecosystem exchange (NEE) in LA was determined to be 0.16ppm by RL22.

Table 1. A subset of the Vulcan 3.0 emission sectors used in this work is presented here. An uncertainty for each sector was determined by proxy data (indicated by "Source"). The temporal resolution of the proxy data and the determined uncertainty are also included in the rightmost columns.

Sector	Source	Resolution	Uncertaint
On-Road	CalTrans Performance Measurement System (PeMS) `pems.dot.ca.gov`	Daily Average	50.00%
Industry	US EPA Greenhouse Gas Reporting Program (GHGRP) `epa.gov/ghgreporting`	Annual Total	38.00%

Marine	Ports of Los Angeles and Long Beach
	Usage Statistics
	`portoflosangeles.org/business/statistics/facts-and-figures`
	`polb.com/business/port-statistics/#latest-statistics`
		Monthly	25.00%

Table 2. A list of errors considered in CO_2 space.

Source of Uncertainty	ε (ppm)	Source
Stochastic Model	0.06	Wu et al., 2018
Boundary Layer Height	0.20	"
Horizontal Wind	1.00	"
Instrument	1.00	Taylor et al., 2020; Kiel et al., 2021
Background	1.00	"
NEE (Bio)	0.16	Wu et al., 2021; Roten, Lin, et al., 2022

2.4 Inversion Method

This work applied an iterative Bayesian inversion to the collection of target/SAM data provided by the OCO-3 instrument. The goal of the optimization process is to minimize a cost function. Here, the cost function is defined such that

$$L_{\mathrm{s}} = \frac{1}{2}(\vec{z} - \mathbf{H}\mathbf{s}_{\mathrm{p}}\vec{\lambda})^{\mathrm{T}}\mathbf{R}^{-1}(\vec{z} - \mathbf{H}\mathbf{s}_{\mathrm{p}}\vec{\lambda}) + \frac{1}{2}(\vec{\lambda} - \vec{\lambda}_{\mathrm{p}})^{\mathrm{T}}\mathbf{Q}_{\mathrm{p}}^{-1}(\vec{\lambda} - \vec{\lambda}_{\mathrm{p}}). \tag{3}$$

Each $XCO_{2,\mathrm{urban}}$ value determined from OCO-3 SAMs is contained in the vector $\vec{z}$. Each corresponding X-STILT footprint is represented as a row in $\mathbf{H}$. The matrix $\mathbf{s}_{\mathrm{p}}$ contains the 10 sector-specific Vulcan fluxes as vectors, with each column representing a different sector. The vector $\vec{\lambda}$ contains "unknown" scaling factors for each sector represented by the columns of $\mathbf{s}_{\mathrm{p}}$. Similarly, $\vec{\lambda}_{\mathrm{p}}$ contains the initial estimate (prior) of scaling factor values. The spatial correlation of errors in XCO_2-space is represented by the $\mathbf{R}$ matrix which has row/column length equal to the number of observations in $\vec{z}$. Following the construction of $\mathbf{R}$ from RL22, elements are defined such that:

$$R_{ij} = \sum_{n} \varepsilon_n^2 \cdot e^{\frac{-X_{ij}}{l}}. \tag{4}$$

Here, ε_n represents the errors in **Table 2**, **X** represents a spatial correlation matrix of the model/observation mismatch for each SAM, and l is a correlation length scale determined by an exponential semi-variogram fitting of the differences. Finally, $\mathbf{Q}_p$ is a diagonal matrix containing the uncertainties corresponding to the elements of $\vec{\lambda}_p$ (see **Table 1**).

The iterative inversion process used in this work applied the cost function to the first SAM in the time series. Updated scaling factors ($\vec{\lambda}$) can be determined by calculating the vector that minimizes the cost function such that

$$\hat{\lambda}_n = \vec{\lambda}_{n-1} + \mathbf{Q}_{\lambda,n-1}\mathbf{K}_n^{\mathrm{T}}(\mathbf{K}_n\mathbf{Q}_{\lambda,n-1}\mathbf{K}_n^{\mathrm{T}} + \mathbf{R}_n)^{-1}(\vec{z}_n - \mathbf{K}_n\vec{\lambda}_{n-1}). \tag{5}$$

Here, $\mathbf{K} = \mathbf{Hs}_p$ is used as a simplification. The iterative notation demonstrates that optimized values determined in $\hat{\lambda}$ were used as $\vec{\lambda}_p$ in the inversion process applied to the next SAM in the series (the initial values in $\vec{\lambda}_p$ were all one). Likewise, updated covariance matrices ($\mathbf{Q}_p$) are calculated by

$$\mathbf{Q}_n = (\mathbf{K}_n^{\mathrm{T}}\mathbf{R}_n^{-1}\mathbf{K}_n + \mathbf{Q}_{n-1}^{-1})^{-1}. \tag{6}$$

3 Results & Discussion

Results from the iterative Bayesian inversion process (**Equations 5** and **6**) are presented for a subset of sectors in **Figure 2**. Posterior scaling factors derived from each SAM are represented by the black points along the time series. The associated uncertainty is represented by the gray bands. Trends in three aforementioned emission sectors show sensitivity to the observations provided by the OCO-3 instrument. Two of these sectors, Industry and On-road, contribute significantly to the total emissions of LA (26% and 42% respectively). Since these sectors are superimposed on several other area sources in the basin, the stronger components will receive priority in the inversion scheme. (Results from all sectors are discussed in the **Supporting Information**.)

Results suggest that the Industry sector was significantly affected by lockdown protocols. Reductions in emissions from this sector were near instantaneous, as effects from local pandemic lockdowns became obvious in early 2020 (Laughner et al., 2021). Given the low temporal resolution of the proxy industrial data, it is unclear if the optimized reductions were a result of the pandemic or a reflection of gradual reductions in CO_2 emissions since 2015 (**Figure 2, Industry**). However, emissions dropped (relative to 2015 levels) shortly after the initial lockdown period. A key characteristic of the industrial sector is that it is made up of both point and area emissions (see **Figure 1, Industry**). Several of the large point sources are situated along the coast and are an order of magnitude larger than the surrounding area sources. Since the proxy data from the GHGRP are point sources only, it is unclear how the inclusion of area sources is affecting the optimized values from the inversion scheme. It is likely that emissions from large point sources are driving the optimized scaling factor for the entire sector (as discussed in RL22). Future work should include provisions in the inversion scheme such that large point sources are treated independently of area sources.

The commercial maritime transportation (Marine) sector shows strong sensitivity to satellite observations provided in the Bayesian inversion scheme. The steady increase in emissions from the marine sector correlates well with the activity reported at two large ports within LA. Although this sector is not a strong contributor to overall emissions from the domain, commercial maritime transportation is the predominant sector just off the coast, with the only other sectors in those gridcells (small-scale maritime vessels) belonging to the non-road sector. Thus the inversion allocates any emission increase to the dominant commercial maritime sector, which has emission hotspots at the port locations.
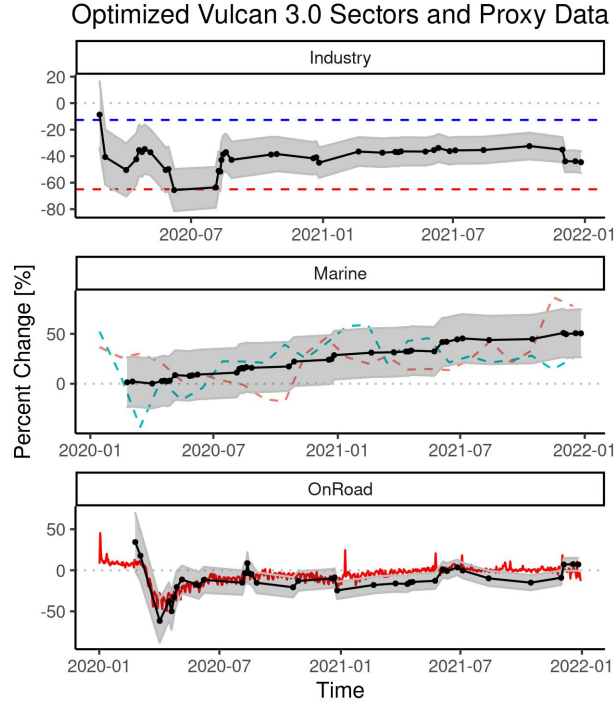
Figure 2. Selected results from a Bayesian inversion assimilation scheme are presented here. SAMs are represented by black points, the temporal trend in the optimized scaling factors is indicated by the black line, and the uncertainty in the optimization is represented by the gray band. Two methods were used to estimate the annual emissions from industrial sectors: (1) the relative change in total emissions from 2015 to 2020 (blue) in point sources in both annual datasets and (2) the total CO_2 reduction from 2015 to 2020 (red). Monthly container totals in the Ports of Los Angeles and Long Beach (relative to 2015 totals) are presented in the marine sector (dashed lines). Daily total vehicle miles traveled were scaled by EPA emission factors to determine the relative difference in CO_2 emissions from the transportation sector (bottom panel, red time-series). Each panel demonstrates that sector-specific trends can be disentangled from space-based XCO_2 observations at a sub-annual scale.

During the months after the onset of the COVID-19 pandemic, commercial maritime traffic experienced longer wait times outside of international ports (Huang et al., 2022; Carter et al., 2022). Emissions from off-shore idling were likely a contributor to this increasing trend.

The effect of the lockdown period is most apparent in the proxy traffic data (**Figure 2, OnRoad**). The on-road sector is the largest contributor within the domain ($\sim$40% of total emissions), making the on-road sector most sensitive to corrections during the inversion process. Daily traffic totals (relative to 2015) demonstrate a clear drop near the beginning of the lockdown period (March, 2022), and optimized emissions follow closely. Furthermore, the increase back to normal traffic levels after spring 2020 is closely tracked by the optimized scaling factors. Although the trends are in good agreement, the system's ability to optimize this sector may be city dependent since denser cities have different transportation dynamics (Wu et al., 2020). While such limitations need to be investigated, this work demonstrates that there is potential for space-based instruments

to detect fluctuations in specific CO_2 sources around the world, making it possible to investigate at the sub-city level in near-real-time.

Although the inversion process doesn't effectively optimize all sectors, the results in **Figure 2** demonstrate that changes in dense space-based XCO_2 observations are capable of being disaggregated into sector-specific contributions. There appear to be two key criteria as to which sectors will be best optimized: (1) the relative strength of the sectors within the domain and (2) the number of sectors that are superimposed within an emission domain of interest. The two highest contributing sectors (On-road and Industry) received the most optimization from the inversion scheme, with the on-road sector tracking the daily proxy data closely. Additionally, one of the minor emission sectors (Marine) was responsive to the inversion scheme due to its predominance along the shore. Any heightened XCO_2 enhancements allocated to this region by X-STILT would be allocated to emissions from the commercial maritime sector.

Previous space-based instruments such as OCO-2 collect soundings in narrow transects during orbit that, when coincident with an urban CO_2 plume, can be used to calculate an enhancement (Wu et al., 2018; Yang et al., 2020). The broad coverage by OCO-3's SAM observations (roughly 80km × 80km) over urban areas reduces the amount of atmospheric mixing that occurs during transport between the source and observation points (soundings), allowing intra-city features to be resolved, thus improving the inversion's ability to optimize specific sectors. Furthermore, OCO-3's ability to collect SAMs at varying times of the day assists in disaggregating sectors with strong diurnal trends.

The results of this work highlight the potential of space-based observations to resolve sector-specific trends in carbon emissions within cities. Developing a global operational framework capable of assimilating data from current and future satellites has the potential to update worldwide emission inventories in near-real-time. Optimized high-resolution emission inventories can potentially reflect the effectiveness of carbon reduction policies at sub-annual time scales. However, shortcomings must be addressed. It is unclear as to how effective this inversion scheme will be when smaller cities are considered. Additionally, potential issues arise when point and area sources are mixed. Posterior scaling factors derived from a collection of independently varying point sources may not accurately scale emissions for all of the considered sources. Therefore, future work should address this shortcoming by assigning each point source a dedicated scaling factor in $\vec{\lambda}$. Obtaining high-resolution proxy data for the industry and/or power generation sectors could provide further insights into the dynamics exhibited by the optimized scaling factors.

4 Conclusions

As the level of atmospheric CO_2 increases, the implementation of local-to-international carbon reduction policies becomes more urgent. Monitoring and reporting emissions from urban areas is difficult with in-situ networks due to their high cost and maintenance, making global coverage unfeasible. Conversely, "bottom-up" accounting approaches (emission inventories) have the potential to provide global estimates of CO_2 emissions but these products can have large uncertainties and often lag several years behind. To remedy these shortcomings, space-based CO_2 observing systems provide near-global coverage of urban areas around the globe. The results of this work demonstrated that observations from such instruments have the potential to optimize sector-specific flux estimates provided by the Vulcan 3.0 emission inventory. In a Bayesian inversion scheme, sectors making up large fractions of the total emissions from the Los Angeles Basin were optimized and posterior values were compared with proxy data. Notably, the strongest two sectors in the basin (on-road transportation and industry) exhibited the most sensitivity to the optimization process. One of the smaller sectors (commercial maritime) also exhibited strong sensitivity. This was due to the lack of coincident sectors. Although several sectors were

optimized and correlated with proxy data, future work should move away from optimizing sectoral scaling factors and expand the inversion scheme to generate posterior percell corrections.

Open Research

All data used to support the conclusions of this work are open source. The locations of all proxy datasets are included in **Table 2.2.3**. The Vulcan 3.0 emission inventory is described by Gurney et al. (2020) and is freely available at `https://daac.ornl.gov/cgi-bin/dsviewer.pl?ds_id=1741`. SMUrF data is described in Wu et al. (2021) and can be found at `https://daac.ornl.gov/NACP/guides/Biogenic_CO2flux_SIF_SMUrF.html`. The X-STILT model used in this work (freely available) is described in Wu et al. (2018) and was driven by the High Resolution Rapid Refresh (HRRR) meteorology data provided by the Air Resources Laboratory (`https://www.ready.noaa.gov/READYmetdata.php`). Data from the OCO-3 instrument can be downloaded from NASA's GES DISC repository (`https://disc.gsfc.nasa.gov/datasets/OCO3_L2_Lite_FP_10.4r/summary`) after registering for a (free) account. All maps were generated using the ggmap package (Kahle & Wickham, 2013).

References

Bares, R., Mitchell, L., Fasoli, B., Bowling, D. R., Catharine, D., Garcia, M., ... Lin, J. C. (2019, August). The utah urban carbon dioxide (UU-CON) and uintah basin greenhouse gas networks: instrumentation, data, and measurement uncertainty. *Earth System Science Data*, *11*(3), 1291–1308. Retrieved from `https://doi.org/10.5194/essd-11-1291-2019` doi: 10.5194/essd-11-1291-2019

Benjamin, S. G., Weygandt, S. S., Brown, J. M., Hu, M., Alexander, C. R., Smirnova, T. G., ... Manikin, G. S. (2016, April). A north american hourly assimilation and model forecast cycle: The rapid refresh. *Monthly Weather Review*, *144*(4), 1669–1694. Retrieved from `https://doi.org/10.1175/mwr-d-15-0242.1` doi: 10.1175/mwr-d-15-0242.1

Carter, C. A., Steinbach, S., & Zhuang, X. (2022, July). Supply chain disruptions and containerized agricultural exports from california ports. *Applied Economic Perspectives and Policy*. Retrieved from `https://doi.org/10.1002/aepp.13311` doi: 10.1002/aepp.13311

Crisp, D., Atlas, R., Breon, F.-M., Brown, L., Burrows, J., Ciais, P., ... Schroll, S. (2004, January). The orbiting carbon observatory (OCO) mission. *Advances in Space Research*, *34*(4), 700–709. Retrieved from `https://doi.org/10.1016/j.asr.2003.08.062` doi: 10.1016/j.asr.2003.08.062

Eldering, A., Taylor, T. E., O'Dell, C. W., & Pavlick, R. (2019, April). The OCO-3 mission: measurement objectives and expected performance based on 1 year of simulated data. *Atmospheric Measurement Techniques*, *12*(4), 2341–2370. Retrieved from `https://doi.org/10.5194/amt-12-2341-2019` doi: 10.5194/amt-12-2341-2019

EPA. (2021, November). *The 2021 automotive trends report* (Tech. Rep. No. EPA-420-R-21-023). United States' Environmental Protection Agency.

Gilfillan, D., & Marland, G. (2021, April). CDIAC-FF: global and national CO_2 emissions from fossil fuel combustion and cement manufacture: 1751–2017. *Earth System Science Data*, *13*(4), 1667–1680. Retrieved from `https://doi.org/10.5194/essd-13-1667-2021` doi: 10.5194/essd-13-1667-2021

Gurney, K. R., Liang, J., Patarasuk, R., Song, Y., Huang, J., & Roest, G. (2020, October). The vulcan version 3.0 high-resolution fossil fuel CO_2 emissions for the united states. *Journal of Geophysical Research: Atmospheres*, *125*(19). Retrieved from `https://doi.org/10.1029/2020jd032974` doi: 10.1029/2020jd032974

Hakkarainen, J., Ialongo, I., & Tamminen, J. (2016, November). Direct space-based observations of anthropogenic CO_2 emission areas from OCO-2. *Geophysical Research Letters*, *43*(21). Retrieved from `https://doi.org/10.1002/2016gl070885` doi: 10.1002/2016gl070885

Hedelius, J. K., Liu, J., Oda, T., Maksyutov, S., Roehl, C. M., Iraci, L. T., ... Wennberg, P. O. (2018, November). Southern california megacity CO_2, CH_4, and CO flux estimates using ground- and space-based remote sensing and a lagrangian model. *Atmospheric Chemistry and Physics*, *18*(22), 16271–16291. Retrieved from `https://doi.org/10.5194/acp-18-16271-2018` doi: 10.5194/acp-18-16271-2018

Huang, L., Tan, Y., & Guan, X. (2022, June). Hub-and-spoke network design for container shipping considering disruption and congestion in the post COVID-19 era. *Ocean & Coastal Management*, *225*, 106230. Retrieved from `https://doi.org/10.1016/j.ocecoaman.2022.106230` doi: 10.1016/j.ocecoaman.2022.106230

Hutchins, M. G., Colby, J. D., Marland, G., & Marland, E. (2016, March). A comparison of five high-resolution spatially-explicit, fossil-fuel, carbon dioxide emission inventories for the united states. *Mitigation and Adaptation Strategies for Global Change*, *22*(6), 947–972. Retrieved from `https://doi.org/10.1007/s11027-016-9709-9` doi: 10.1007/s11027-016-9709-9

Intergovernmental Panel on Climate Change. (2015). *Climate change 2014: Mitigation of climate change.* Cambridge, England: Cambridge University Press.

Janssens-Maenhout, G., Crippa, M., Guizzardi, D., Muntean, M., Schaaf, E., Dentener, F., ... Oreggioni, G. D. (2019, July). EDGAR v4.3.2 global atlas of the three major greenhouse gas emissions for the period 1970–2012. *Earth System Science Data*, *11*(3), 959–1002. Retrieved from `https://doi.org/10.5194/essd-11-959-2019` doi: 10.5194/essd-11-959-2019

Janssens-Maenhout, G., Pinty, B., Dowell, M., Zunker, H., Andersson, E., Balsamo, G., ... Veefkind, P. (2020, August). Toward an operational anthropogenic CO2 emissions monitoring and verification support capacity. *Bulletin of the American Meteorological Society*, *101*(8), E1439–E1451. Retrieved from `https://doi.org/10.1175/bams-d-19-0017.1` doi: 10.1175/bams-d-19-0017.1

Kahle, D., & Wickham, H. (2013). ggmap: Spatial visualization with ggplot2. *The R Journal*, *5*(1), 144–161. Retrieved from `https://journal.r-project.org/archive/2013-1/kahle-wickham.pdf`

Keppel-Aleks, G., Wennberg, P. O., & Schneider, T. (2011, April). Sources of variations in total column carbon dioxide. *Atmospheric Chemistry and Physics*, *11*(8), 3581–3593. Retrieved from `https://doi.org/10.5194/acp-11-3581-2011` doi: 10.5194/acp-11-3581-2011

Kiel, M., Eldering, A., Roten, D. D., Lin, J. C., Feng, S., Lei, R., ... Iraci, L. T. (2021, June). Urban-focused satellite CO_2 observations from the orbiting carbon observatory-3: A first look at the los angeles megacity. *Remote Sensing of Environment*, *258*, 112314. Retrieved from `https://doi.org/10.1016/j.rse.2021.112314` doi: 10.1016/j.rse.2021.112314

Kunik, L., Mallia, D. V., Gurney, K. R., Mendoza, D. L., Oda, T., & Lin, J. C.

(2019, January). Bayesian inverse estimation of urban CO_2 emissions: Results from a synthetic data simulation over salt lake city, UT. *Elementa: Science of the Anthropocene*, *7*. Retrieved from `https://doi.org/10.1525/elementa.375` doi: 10.1525/elementa.375

Laughner, J. L., Neu, J. L., Schimel, D., Wennberg, P. O., Barsanti, K., Bowman, K. W., . . . and, Z.-C. Z. (2021, November). Societal shifts due to COVID-19 reveal large-scale complexities and feedbacks between atmospheric chemistry and climate change. *Proceedings of the National Academy of Sciences*, *118*(46). Retrieved from `https://doi.org/10.1073/pnas.2109481118` doi: 10.1073/pnas.2109481118

Lauvaux, T., Gurney, K. R., Miles, N. L., Davis, K. J., Richardson, S. J., Deng, A., . . . Turnbull, J. (2020, August). Policy-relevant assessment of urban CO_2 emissions. *Environmental Science & Technology*, *54*(16), 10237–10245. Retrieved from `https://doi.org/10.1021/acs.est.0c00343` doi: 10.1021/acs.est.0c00343

Lauvaux, T., Miles, N. L., Deng, A., Richardson, S. J., Cambaliza, M. O., Davis, K. J., . . . Wu, K. (2016, May). High-resolution atmospheric inversion of urban CO_2 emissions during the dormant season of the indianapolis flux experiment (INFLUX). *Journal of Geophysical Research: Atmospheres*, *121*(10), 5213–5236. Retrieved from `https://doi.org/10.1002/2015jd024473` doi: 10.1002/2015jd024473

Lu, S., Wang, J., Wang, Y., & Yan, J. (2018, March). Analysis on the variations of atmospheric CO_2 concentrations along the urban–rural gradients of chinese cities based on the OCO-2 XCO data. *International Journal of Remote Sensing*, *39*(12), 4194–4213. Retrieved from `https://doi.org/10.1080/01431161.2017.1415482` doi: 10.1080/01431161.2017.1415482

Mallia, D. V., Mitchell, L. E., Kunik, L., Fasoli, B., Bares, R., Gurney, K. R., . . . Lin, J. C. (2020, December). Constraining urban CO_2 emissions using mobile observations from a light rail public transit platform. *Environmental Science & Technology*, *54*(24), 15613–15621. Retrieved from `https://doi.org/10.1021/acs.est.0c04388` doi: 10.1021/acs.est.0c04388

Miller, J. B., Lehman, S. J., Verhulst, K. R., Miller, C. E., Duren, R. M., Yadav, V., . . . Sloop, C. D. (2020, October). Large and seasonally varying biospheric CO_2 fluxes in the los angeles megacity revealed by atmospheric radiocarbon. *Proceedings of the National Academy of Sciences*, *117*(43), 26681–26687. Retrieved from `https://doi.org/10.1073/pnas.2005253117` doi: 10.1073/pnas.2005253117

Oda, T., Maksyutov, S., & Andres, R. J. (2018, January). The open-source data inventory for anthropogenic CO_2, version 2016 (ODIAC2016): a global monthly fossil fuel CO_2 gridded emissions data product for tracer transport simulations and surface flux inversions. *Earth System Science Data*, *10*(1), 87–107. Retrieved from `https://doi.org/10.5194/essd-10-87-2018` doi: 10.5194/essd-10-87-2018

Rayner, P. J., & O'Brien, D. M. (2001, January). The utility of remotely sensed CO_2 concentration data in surface source inversions. *Geophysical Research Letters*, *28*(1), 175–178. Retrieved from `https://doi.org/10.1029/2000gl011912` doi: 10.1029/2000gl011912

Rodgers, C. D. (2000). *Inverse methods for atmospheric sounding*. WORLD SCIENTIFIC. Retrieved from `https://doi.org/10.1142/3171` doi: 10.1142/3171

Roten, D., Lin, J. C., Kunik, L., Mallia, D., Wu, D., Oda, T., & Kort, E. A. (2022, May). The information content of dense carbon dioxide measurements from space: A high-resolution inversion approach with synthetic data from the OCO-3 instrument. *Atmospheric Chemistry and Physics*. Retrieved from `https://doi.org/10.5194/acp-2022-315` doi: 10.5194/acp-2022-315

Roten, D., Marland, G., Bun, R., Crippa, M., Gilfillan, D., Jones, M., . . . Andrew,

R. (2022, March 14). Co2 emissions from energy systems and industrial processes: Inventories from data- and proxy-driven approaches. In *Balancing greenhouse gas budgets* (1st ed.). Netherlands: Elsevier.

Shekhar, A., Chen, J., Paetzold, J. C., Dietrich, F., Zhao, X., Bhattacharjee, S., . . . Wofsy, S. C. (2020, September). Anthropogenic CO_2 emissions assessment of nile delta using XCO_2 and SIF data from OCO-2 satellite. *Environmental Research Letters*, *15*(9), 095010. Retrieved from `https://doi.org/10.1088/1748-9326/ab9cfe` doi: 10.1088/1748-9326/ab9cfe

Shusterman, A. A., Teige, V. E., Turner, A. J., Newman, C., Kim, J., & Cohen, R. C. (2016, October). The BErkeley atmospheric CO_2 observation network: initial evaluation. *Atmospheric Chemistry and Physics*, *16*(21), 13449–13463. Retrieved from `https://doi.org/10.5194/acp-16-13449-2016` doi: 10.5194/acp-16-13449-2016

Taylor, T. E., Eldering, A., Merrelli, A., Kiel, M., Somkuti, P., Cheng, C., . . . Yu, S. (2020, December). OCO-3 early mission operations and initial (vEarly) XCO_2 and SIF retrievals. *Remote Sensing of Environment*, *251*, 112032. Retrieved from `https://doi.org/10.1016/j.rse.2020.112032` doi: 10.1016/j.rse.2020.112032

Turner, A. J., Kim, J., Fitzmaurice, H., Newman, C., Worthington, K., Chan, K., . . . Cohen, R. C. (2020, November). Observed impacts of COVID-19 on urban CO_2 emissions. *Geophysical Research Letters*, *47*(22). Retrieved from `https://doi.org/10.1029/2020gl090037` doi: 10.1029/2020gl090037

Wu, D., Lin, J. C., Duarte, H. F., Yadav, V., Parazoo, N. C., Oda, T., & Kort, E. A. (2021, June). A model for urban biogenic CO_2 fluxes: Solar-induced fluorescence for modeling urban biogenic fluxes (SMUrF v1). *Geoscientific Model Development*, *14*(6), 3633–3661. Retrieved from `https://doi.org/10.5194/gmd-14-3633-2021` doi: 10.5194/gmd-14-3633-2021

Wu, D., Lin, J. C., Fasoli, B., Oda, T., Ye, X., Lauvaux, T., . . . Kort, E. A. (2018, December). A lagrangian approach towards extracting signals of urban CO_2 emissions from satellite observations of atmospheric column CO_2 (XCO_2): X-stochastic time-inverted lagrangian transport model ("x-STILT v1"). *Geoscientific Model Development*, *11*(12), 4843–4871. Retrieved from `https://doi.org/10.5194/gmd-11-4843-2018` doi: 10.5194/gmd-11-4843-2018

Wu, D., Lin, J. C., Oda, T., & Kort, E. A. (2020, February). Space-based quantification of per capita CO_2 emissions from cities. *Environmental Research Letters*, *15*(3), 035004. Retrieved from `https://doi.org/10.1088/1748-9326/ab68eb` doi: 10.1088/1748-9326/ab68eb

Yang, E. G., Kort, E. A., Wu, D., Lin, J. C., Oda, T., Ye, X., & Lauvaux, T. (2020, April). Using space-based observations and lagrangian modeling to evaluate urban carbon dioxide emissions in the middle east. *Journal of Geophysical Research: Atmospheres*, *125*(7). Retrieved from `https://doi.org/10.1029/2019jd031922` doi: 10.1029/2019jd031922

Ye, X., Lauvaux, T., Kort, E. A., Oda, T., Feng, S., Lin, J. C., . . . Wu, D. (2020, April). Constraining fossil fuel CO_2 emissions from urban area using OCO-2 observations of total column CO_2. *Journal of Geophysical Research: Atmospheres*, *125*(8). Retrieved from `https://doi.org/10.1029/2019jd030528` doi: 10.1029/2019jd030528

Zhong, W., & Haigh, J. D. (2013, March). The greenhouse effect and carbon dioxide. *Weather*, *68*(4), 100–105. Retrieved from `https://doi.org/10.1002/wea.2072` doi: 10.1002/wea.2072

Constraining Sector-specific CO_2 Fluxes using Space-based XCO_2 Observations over the Los Angeles Basin

Dustin Roten[1], John C. Lin[2], Eric A. Kort[3]

[1] Jet Propulsion Laboratory, California Institute of Technology, Pasadena, CA, USA
[2] Department of Atmospheric Sciences, University of Utah, Salt Lake City, UT, USA
[3] Climate and Space Sciences and Engineering, University of Michigan, Ann Arbor, MI, USA

Key Points:

- NASA's OCO-3 instrument provides the densest spatial coverage of urban XCO_2 from space, which includes information on spatially variant surface fluxes. We show this spatial coverage makes it possible to disaggregate sectoral emissions information from observations.
- Using OCO-3 and the Los Angeles Basin as a case study, three emission sectors from an emission inventory are optimized to include effects from COVID-19 lockdowns. In two contributing sectors, On-road Transportation and Industry, optimized CO_2 flux decreased considerably around the time COVID-19 lockdowns were implemented in the Los Angeles area. In the third sector, Maritime Transportation, optimized CO_2 flux steadily increased over time.
- The timeseries of optimized fluxes followed sector-specific proxy data.

Corresponding author: Dustin Roten, `droten@jpl.nasa.gov`

Abstract

The concentration of carbon dioxide (CO_2) in Earth's atmosphere is increasing due to human activities and the resulting effects on the global climate system have initiated several policy-driven approaches to reduce emissions of this greenhouse gas. Quantifying the effectiveness of such policies requires both bottom-up and top-down approaches to estimate CO_2 emissions. This work investigates, for the first time, the potential of using SAM observations from NASA's OCO-3 instrument to disaggregate sector-specific emissions from instrument observations. Optimized sector-specific timeseries were produced using Bayesian inversion techniques and compared to proxy activity data from the transportation, commercial maritime, and industrial sectors. Results demonstrate that dense space-based observations of atmospheric CO_2 are capable of disentangling sector-specific CO_2 fluxes, paving the way for accurate monitoring of the effects of carbon-reduction policies and operational carbon monitoring systems.

Plain Language Summary

Carbon dioxide (CO_2) is a key greenhouse gas and several local-to-international policies are in place to reduce the amount being emitted by human activities. This work investigates the amount of CO_2 emitted within the Los Angeles Basin during the period between January 2020 and December 2021 using NASA's Orbiting Carbon Observatory-3. The observed emissions are broken down into contributions from specific sectors (on-road transportation, industrial sources, commercial maritime activity, etc.) The results of this work demonstrate that urban CO_2 emissions observed from space-based instrumentation can be disaggregated to several socioeconomic sectors to study trends that may be present in each one. Notable detected features include the sudden reduction of on-road CO_2 emissions due to the COVID-19 lockdown period and the steady increase in off-shore emissions due to ship idling and delays. The effectiveness of current and future policies regarding sector-specific reductions have the potential to be observed over time using the framework presented here.

1 Introduction

Carbon dioxide from the combustion of fossil fuels ($FFCO_2$) is among the most important greenhouse gases in the atmosphere (Zhong & Haigh, 2013). Anthropogenic activities typically associated with cities are a significant source (Intergovernmental Panel on Climate Change, 2015). Efforts to constrain estimates of these emissions use two methods: "bottom-up" inventory estimates and "top-down" atmospheric observations. Bottom-up methods use a variety of activity data and statistical methods to construct approximate distributions of $FFCO_2$ fluxes across many geographic scales (Oda et al., 2018; Janssens-Maenhout et al., 2019; Gurney et al., 2020; Gilfillan & Marland, 2021). However, this reliance on multiple data streams often delays the release of updated inventories, as many sources have coarse temporal resolution and/or take time to update (Roten, Marland, et al., 2022). Furthermore, variations in construction methods create substantial differences between inventories (Hutchins et al., 2016). Some cities host ground-based (top-down) CO_2 observing networks that record atmospheric measurements at a high temporal resolution. While these observations provide a means to constrain the "true" magnitude of emissions from urban areas and validate inventories, these networks are limited to a handful of cities, have few instrument sites, and require sophisticated interpretation to disentangle urban signals (Bares et al., 2019; Lauvaux et al., 2016; Shusterman et al., 2016). Results from both methods are used to inform carbon cycle science and reduction policies at local, national, and international scales.

Space-based carbon-observing instruments are providing routine observations at near-global coverage with revisit times ranging from three to 16 days (Janssens-Maenhout et al., 2020). These increases in spatiotemporal coverage address the shortcomings of cur-

rent bottom-up and top-down methodologies. As observations are collected over time, spatial gradients and localized enhancements are revealed, driven by emissions from populated areas (Hakkarainen et al., 2016). Although the signals detected by space-based instruments are inherently attenuated due to column-averaging (Rayner & O'Brien, 2001; Keppel-Aleks et al., 2011), these observations are capable of providing insights into localized urban emissions. Many studies show that transects obtained by NASA's Orbiting Carbon Observatory-2 (OCO-2) near urban areas are useful in constraining local CO_2 emissions (Lu et al., 2018; Hedelius et al., 2018; Wu et al., 2018; Yang et al., 2020; Wu et al., 2020) even though the original intent of this instrument was to inform carbon cycle science at regional/global scale (Crisp et al., 2004).

The installation of OCO-3 on the International Space Station (ISS) in 2019 allows for the collection of spatially dense soundings over targeted urban areas. This new type of observation, referred to as "Snapshot Area Maps" (SAMs), covers a domain of roughly 80km × 80km with individual atmospheric soundings spaced roughly 2km apart (Eldering et al., 2019). This increased density allows sub-city spatial features to be resolved in XCO_2-space and provides more emission information than other space-based instruments (Kiel et al., 2021). Furthermore, the orbit of the ISS allows SAMs to be collected at varying daytime hours as opposed to the narrow time window (around 1:30pm local time) that previous instruments such as OCO-2 are restricted to (Crisp et al., 2004; Eldering et al., 2019). Using Bayesian inversion techniques (Rodgers, 2000), these sub-city enhancements can inform the construction of emission inventories that represent surface emissions in flux-space (Roten, Lin, et al., 2022) (referred to hereafter as RL22). RL22 provides a "first look" into the potential of using OCO-3 SAMs to optimize sector-specific urban flux estimates by constructing an observing system simulation experiment (OSSE). Their results suggest that individual SAMs provide minimal spatial optimization of prior inventories while aggregating SAMs over time generated useful scaling factors for sector-specific emission estimates.

Although Bayesian methods are frequently applied to ground-based CO_2 networks (Kunik et al., 2019; Mallia et al., 2020; Turner et al., 2020; Lauvaux et al., 2020), the number of applications using XCO_2 observations is growing (Ye et al., 2020; Shekhar et al., 2020). For instance, Ye et al. (2020) used OCO-2 observations over the Los Angeles Basin to calculate optimized scaling factors for emissions estimates provided by the ODIAC inventory (Oda et al., 2018) with factors ranging from 0.66 to 1.84. While previous studies focused on optimizing total emissions from a "whole-city" perspective, this work demonstrates the potential of disaggregating sector-specific contributions to CO_2 enhancements measured from a space-based instrument in near-real-time. Timeseries of optimized emissions from sector-specific sources were compared with hourly roadway traffic, monthly marine activity, and annual industry emission data and show good agreement with expected trends. Decreases in emissions during LA's COVID-19 lockdowns (Laughner et al., 2021) were also detected by OCO-3. Results demonstrate that space-based XCO_2 observations are capable of optimizing multiple emission sectors within the LA domain, highlighting the importance of regular high-resolution measurements for the purposes of constraining sector-specific emissions and quantifying the short-term effectiveness of sector-specific carbon reduction policies. Additionally, the techniques presented in this work show potential to be applied broadly to multiple cities around the world, providing a piece of the framework for a global near-real-time carbon monitoring system.

2 Methods

2.1 Study Domain: The Los Angeles Basin

The United States Census Bureau reports that the Los Angeles metro area is home to roughly 13 million people. This megacity sits along the southern California coast and

has two active maritime ports, multiple international airports, and several traversing interstate highways. This area hosts large coastal industrial complexes and sizable power plants to the south. The CO_2 emission domain considered in this work covers much of the Basin area, including the San Fernando and San Bernardino Valleys (see **Figure 1 (top)**). OCO-3 has collected more than 50 target and SAM observations over this area between 8:00am and 6:00pm local time. Each sounding making up these SAMs is treated as an independent observation of column-averaged CO_2 ($XCO_{2,obs}$) and is assumed to be the summation of three components:

$$XCO_{2,obs} = XCO_{2,urban} + XCO_{2,bkg} + XCO_{2,bio:urban}. \tag{1}$$

$XCO_{2,urban}$ is the fossil contribution from the urban domain of interest, $XCO_{2,bkg}$ is the contribution from residual sources (anthropogenic and biospheric) outside of the domain, and $XCO_{2,bio:urban}$ is the biospheric impact on $XCO_{2,urban}$. Isolating $XCO_{2,urban}$ of each sounding and comparing it to modeled estimates provides the constraint on the emission estimate. Additionally, $XCO_{2,bkg}$ can be further broken down into two terms:

$$XCO_{2,bkg} = XCO_{2,bkg:bio} + XCO_{2,bkg:other}. \tag{2}$$

Here, $XCO_{2,bkg:bio}$ represents the influence that the biosphere has on the background estimation and $XCO_{2,bkg:other}$ represents the remainder.

Surface CO_2 flux from the domain was represented by the Vulcan 3.0 emission inventory (Gurney et al., 2020) using the latest available year (2015). This spatially explicit emission inventory contains 10 sectors that span residential, commercial, and industrial sources at a 1km $\times$ 1km resolution. The on-road transportation sector is responsible for almost half (42%) of the urban emissions from LA followed by the industrial (26%). A weaker yet important source is the commercial maritime sector (2%), which is confined along the coast of the LA and is not coincident with other significant emission sectors. The spatial distribution of the on-road, industrial, and marine sectors are included in **Figure 1 (bottom)**. (Spatial plots of emissions from other sectors are included in the **Supporting Information**.)

Individual XCO_2 soundings are irregularly gridded across the domain and are affected by clouds, aerosols, and viewing geometry (Eldering et al., 2019). Using the column-averaged Stochastic Time-Inverted Lagrangian Transport (X-STILT) model (Wu et al., 2018), an influence footprint was generated for each good quality sounding across all SAMs (see RL22 for further information regarding the setup of this model for LA). These X-STILT footprints were convolved with the Vulcan 3.0 emission inventory to calculate modeled $XCO_{2,urban}$ values at each sounding location. Soundings where the contribution from LA was ≤ 0.01ppm, as calculated by X-STILT, identified "background" soundings for each SAM. The average of these soundings was used as $XCO_{2,bkg}$. Biospheric influences, making up $\sim$20% of the variability in the LA region (Miller et al., 2020), were incorporated with the Solar-Induced Fluorescence for Modeling Urban Biogenic Fluxes (SMUrF) model (Wu et al., 2021). Using observations of solar-induced fluorescence from space, SMUrF generates a spatially explicit inventory of the hourly net ecosystem exchange of CO_2. Footprints were convolved with SMUrF output to remove per sounding biospheric influences ($XCO_{2,bio:urban}$ and $XCO_{2,bio:bkg}$).

2.2 Proxy Data and Uncertainty

Although estimated CO_2 flux is provided at an hourly timescale, the Vulcan 3.0 emission inventory only provides spatially explicit high and low estimates (uncertainties) of these fluxes at an annual scale (Gurney et al., 2020). For each cell, the maximum of
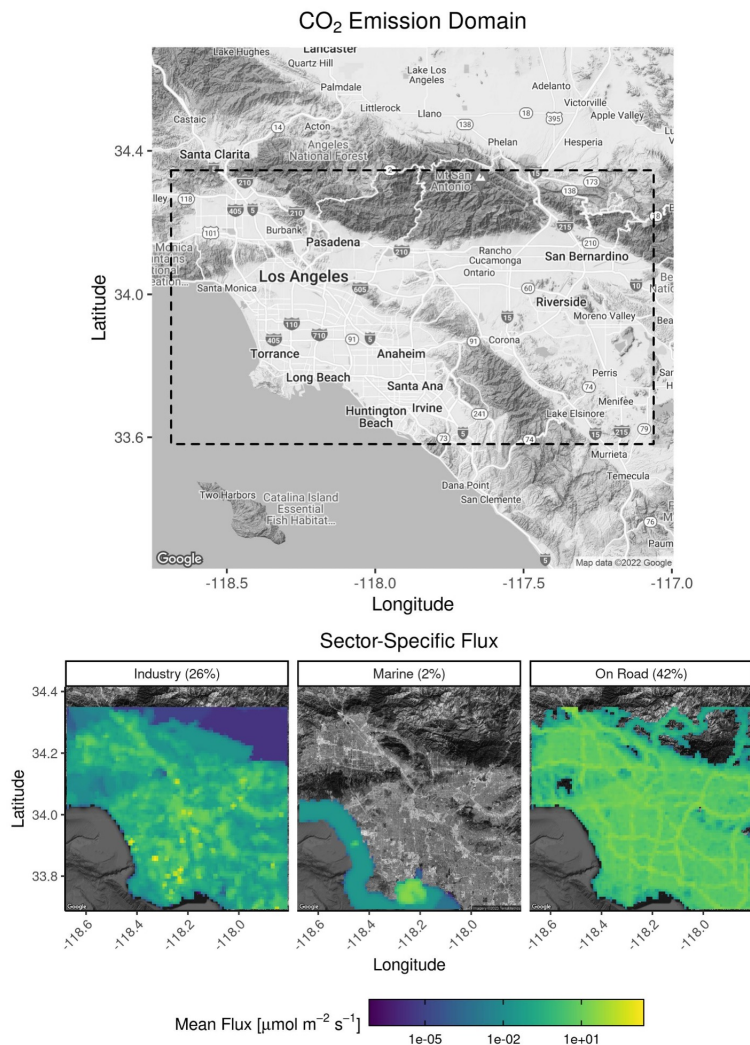
CO$_2$ Emission Domain

Sector-Specific Flux

Figure 1. A description of the domain of interest. The urban domain includes the Los Angeles Basin, San Fernando Valley, and San Bernardino Valley (black rectangle, top). The spatial distribution of selected sectoral emissions from Vulcan 3.0 are presented in the bottom panels (emission estimates are from year 2015).

the absolute differences between these high/low estimates was used to assign an uncertainty estimate. The sum of these per-cell values provided an overall uncertainty estimate for each sector. While this methodology reflected typical uncertainty values, changes in socioeconomic dynamics due to the COVID-19 pandemic influenced CO$_2$ fluxes considerably (Laughner et al., 2021). The initial uncertainties derived from annual Vulcan 3.0 estimates are averaged from a typical year of emissions. No sudden socioeconomic changes were present in these estimates, suggesting that they were underestimates when applied to the 2020/2021 time frame. To address this shortcoming, independent sources of activity data were used to calculate alternative uncertainty values for several sectors. These values specifically incorporated socioeconomic fluctuations from the COVID-19 pandemic and replaced previously calculated uncertainty estimates when possible. Descriptions of the available activity data relevant to the on-road, industrial, and marine

sectors are presented below and summarized in **Table 1**. (Discussion of proxy data beyond the primary sectors featured here are included in the **Supporting Information**.)

2.2.1 On-road Transportation

There are efforts to record trends in several economic sectors in LA. A notable example is the California Department of Transportation's Performance Measurement System (PeMS) which uses an array of sensors to collect traffic data from the interstate highways throughout the state. In this work, data from five highways traversing the basin (10, 105, 210, 405, 605) were aggregated to produce daily total traffic counts for years 2015, 2020, and 2021. These values were then multiplied by average annual per-mile CO_2 emissions factors from the EPA (EPA, 2021). The daily percent change from 2015 was calculated by comparing each day of the 2020/2021 time period to its corresponding day in 2015. Comparing weekdays and weekend days to corresponding days in 2015 eliminated weekday/weekend mismatch. The maximum change in on-road activity during the 2020/2021 time period occurred during March 2020 with a reduction of roughly 50%.

2.2.2 Industry

The U.S. Environmental Protection Agency (US EPA) provides annual datasets for large point source emitters. The dataset used in this work is from the Greenhouse Gases Reporting Program (GHGRP). It includes voluntarily reported CO_2 emissions from point sources beyond power generation facilities (such as large industrial manufacturers). Due to the voluntary nature of GHGRP reporting, point sources reported in 2015 are not guaranteed to be included in 2020/2021. Comparing annual totals between 2015 and 2020 revealed a 60% reduction from these point sources. In an alternative calculation, using only point sources present in both datasets, GHGRP revealed a reduction of 12%. Using annual totals, Vulcan 3.0 provides a maximum difference of 38%. This intermediate value was used as the uncertainty for the industrial sector.

2.2.3 Marine

The Ports of Los Angeles and Long Beach maintain monthly records of port activity through container movement. Monthly trends in passenger and cargo totals in 2020/2021 were compared to base values from 2015. During the span of 2020, a steady increase in passenger and cargo activity at both ports is evident.

2.3 Errors in XCO$_2$-space

The Bayesian inversion scheme requires uncertainties in both prior fluxes and observations. Both of which are used in the construction of posterior scaling factors for each sector. Mismatches in modeled and observed XCO_2 values stem from the stochastic nature of the X-STILT model, improper characterization of the boundary layer height, errors in the horizontal wind speed/direction, instrument limitations, and uncertainty from the biospheric model. Wu et al. (2018) quantified transport uncertainties in the X-STILT model using global, low-resolution meteorological data while the meteorological fields used in this study were provided by the 3km High Resolution Rapid Refresh (HRRR) dataset (Benjamin et al., 2016). The uncertainties from the lower resolution meteorological fields from Wu et al. (2018) are included in **Table 2** and are assumed to be overestimates of HRRR uncertainties. Additionally, multiple studies have characterized OCO-3's retrieval error at both the local (LA) and global levels (Kiel et al., 2021; Taylor et al., 2020) where values range from 0.23 to 2ppm. A mid-range value of 1ppm was selected to represent the instrument error over LA area. Uncertainty in the net ecosystem exchange (NEE) in LA was determined to be 0.16ppm by RL22.

Table 1. A subset of the Vulcan 3.0 emission sectors used in this work is presented here. An uncertainty for each sector was determined by proxy data (indicated by "Source"). The temporal resolution of the proxy data and the determined uncertainty are also included in the rightmost columns.

Sector	Source	Resolution	Uncertaint
On-Road	CalTrans Performance Measurement System (PeMS) `pems.dot.ca.gov`	Daily Average	50.00%
Industry	US EPA Greenhouse Gas Reporting Program (GHGRP) `epa.gov/ghgreporting`	Annual Total	38.00%

Marine	Ports of Los Angeles and Long Beach
	Usage Statistics
	`portoflosangeles.org/business/statistics/facts-and-figures`
	`polb.com/business/port-statistics/#latest-statistics`
		Monthly	25.00%

Table 2. A list of errors considered in CO_2 space.

Source of Uncertainty	ε (ppm)	Source
Stochastic Model	0.06	Wu et al., 2018
Boundary Layer Height	0.20	"
Horizontal Wind	1.00	"
Instrument	1.00	Taylor et al., 2020; Kiel et al., 2021
Background	1.00	"
NEE (Bio)	0.16	Wu et al., 2021; Roten, Lin, et al., 2022

2.4 Inversion Method

This work applied an iterative Bayesian inversion to the collection of target/SAM data provided by the OCO-3 instrument. The goal of the optimization process is to minimize a cost function. Here, the cost function is defined such that

$$L_{\mathrm{s}} = \frac{1}{2}(\vec{z} - \mathbf{H}\mathbf{s}_{\mathrm{p}}\vec{\lambda})^{\mathrm{T}}\mathbf{R}^{-1}(\vec{z} - \mathbf{H}\mathbf{s}_{\mathrm{p}}\vec{\lambda}) + \frac{1}{2}(\vec{\lambda} - \vec{\lambda}_{\mathrm{p}})^{\mathrm{T}}\mathbf{Q}_{\mathrm{p}}^{-1}(\vec{\lambda} - \vec{\lambda}_{\mathrm{p}}). \tag{3}$$

Each $XCO_{2,\mathrm{urban}}$ value determined from OCO-3 SAMs is contained in the vector $\vec{z}$. Each corresponding X-STILT footprint is represented as a row in $\mathbf{H}$. The matrix $\mathbf{s}_{\mathrm{p}}$ contains the 10 sector-specific Vulcan fluxes as vectors, with each column representing a different sector. The vector $\vec{\lambda}$ contains "unknown" scaling factors for each sector represented by the columns of $\mathbf{s}_{\mathrm{p}}$. Similarly, $\vec{\lambda}_{\mathrm{p}}$ contains the initial estimate (prior) of scaling factor values. The spatial correlation of errors in XCO_2-space is represented by the $\mathbf{R}$ matrix which has row/column length equal to the number of observations in $\vec{z}$. Following the construction of $\mathbf{R}$ from RL22, elements are defined such that:

$$R_{ij} = \sum_{n} \varepsilon_n^2 \cdot e^{\frac{-X_{ij}}{l}}. \tag{4}$$

Here, ε_n represents the errors in **Table 2**, **X** represents a spatial correlation matrix of the model/observation mismatch for each SAM, and l is a correlation length scale determined by an exponential semi-variogram fitting of the differences. Finally, $\mathbf{Q}_p$ is a diagonal matrix containing the uncertainties corresponding to the elements of $\vec{\lambda}_p$ (see **Table 1**).

The iterative inversion process used in this work applied the cost function to the first SAM in the time series. Updated scaling factors ($\hat{\lambda}$) can be determined by calculating the vector that minimizes the cost function such that

$$\hat{\lambda}_n = \vec{\lambda}_{n-1} + \mathbf{Q}_{\lambda,n-1}\mathbf{K}_n^T(\mathbf{K}_n\mathbf{Q}_{\lambda,n-1}\mathbf{K}_n^T + \mathbf{R}_n)^{-1}(\vec{z}_n - \mathbf{K}_n\vec{\lambda}_{n-1}). \tag{5}$$

Here, $\mathbf{K} = \mathbf{H}\mathbf{s}_p$ is used as a simplification. The iterative notation demonstrates that optimized values determined in $\hat{\lambda}$ were used as $\vec{\lambda}_p$ in the inversion process applied to the next SAM in the series (the initial values in $\vec{\lambda}_p$ were all one). Likewise, updated covariance matrices ($\mathbf{Q}_p$) are calculated by

$$\mathbf{Q}_n = (\mathbf{K}_n^T\mathbf{R}_n^{-1}\mathbf{K}_n + \mathbf{Q}_{n-1}^{-1})^{-1}. \tag{6}$$

3 Results & Discussion

Results from the iterative Bayesian inversion process (**Equations 5** and **6**) are presented for a subset of sectors in **Figure 2**. Posterior scaling factors derived from each SAM are represented by the black points along the time series. The associated uncertainty is represented by the gray bands. Trends in three aforementioned emission sectors show sensitivity to the observations provided by the OCO-3 instrument. Two of these sectors, Industry and On-road, contribute significantly to the total emissions of LA (26% and 42% respectively). Since these sectors are superimposed on several other area sources in the basin, the stronger components will receive priority in the inversion scheme. (Results from all sectors are discussed in the **Supporting Information**.)

Results suggest that the Industry sector was significantly affected by lockdown protocols. Reductions in emissions from this sector were near instantaneous, as effects from local pandemic lockdowns became obvious in early 2020 (Laughner et al., 2021). Given the low temporal resolution of the proxy industrial data, it is unclear if the optimized reductions were a result of the pandemic or a reflection of gradual reductions in CO_2 emissions since 2015 (**Figure 2, Industry**). However, emissions dropped (relative to 2015 levels) shortly after the initial lockdown period. A key characteristic of the industrial sector is that it is made up of both point and area emissions (see **Figure 1, Industry**). Several of the large point sources are situated along the coast and are an order of magnitude larger than the surrounding area sources. Since the proxy data from the GHGRP are point sources only, it is unclear how the inclusion of area sources is affecting the optimized values from the inversion scheme. It is likely that emissions from large point sources are driving the optimized scaling factor for the entire sector (as discussed in RL22). Future work should include provisions in the inversion scheme such that large point sources are treated independently of area sources.

The commercial maritime transportation (Marine) sector shows strong sensitivity to satellite observations provided in the Bayesian inversion scheme. The steady increase in emissions from the marine sector correlates well with the activity reported at two large ports within LA. Although this sector is not a strong contributor to overall emissions from the domain, commercial maritime transportation is the predominant sector just off the coast, with the only other sectors in those gridcells (small-scale maritime vessels) belonging to the non-road sector. Thus the inversion allocates any emission increase to the dominant commercial maritime sector, which has emission hotspots at the port locations.
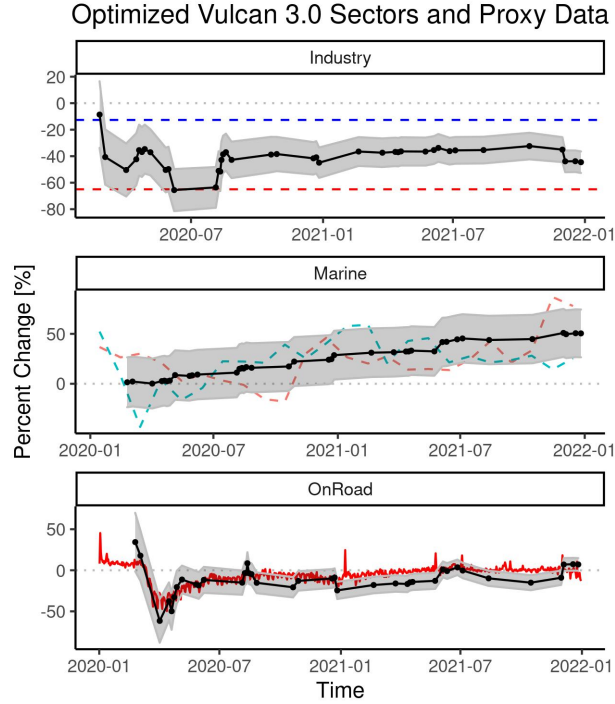
Figure 2. Selected results from a Bayesian inversion assimilation scheme are presented here. SAMs are represented by black points, the temporal trend in the optimized scaling factors is indicated by the black line, and the uncertainty in the optimization is represented by the gray band. Two methods were used to estimate the annual emissions from industrial sectors: (1) the relative change in total emissions from 2015 to 2020 (blue) in point sources in both annual datasets and (2) the total CO_2 reduction from 2015 to 2020 (red). Monthly container totals in the Ports of Los Angeles and Long Beach (relative to 2015 totals) are presented in the marine sector (dashed lines). Daily total vehicle miles traveled were scaled by EPA emission factors to determine the relative difference in CO_2 emissions from the transportation sector (bottom panel, red timeseries). Each panel demonstrates that sector-specific trends can be disentangled from space-based XCO_2 observations at a sub-annual scale.

During the months after the onset of the COVID-19 pandemic, commercial maritime traffic experienced longer wait times outside of international ports (Huang et al., 2022; Carter et al., 2022). Emissions from off-shore idling were likely a contributor to this increasing trend.

The effect of the lockdown period is most apparent in the proxy traffic data (**Figure 2, OnRoad**). The on-road sector is the largest contributor within the domain ($\sim$40% of total emissions), making the on-road sector most sensitive to corrections during the inversion process. Daily traffic totals (relative to 2015) demonstrate a clear drop near the beginning of the lockdown period (March, 2022), and optimized emissions follow closely. Furthermore, the increase back to normal traffic levels after spring 2020 is closely tracked by the optimized scaling factors. Although the trends are in good agreement, the system's ability to optimize this sector may be city dependent since denser cities have different transportation dynamics (Wu et al., 2020). While such limitations need to be investigated, this work demonstrates that there is potential for space-based instruments

to detect fluctuations in specific CO_2 sources around the world, making it possible to investigate at the sub-city level in near-real-time.

Although the inversion process doesn't effectively optimize all sectors, the results in **Figure 2** demonstrate that changes in dense space-based XCO_2 observations are capable of being disaggregated into sector-specific contributions. There appear to be two key criteria as to which sectors will be best optimized: (1) the relative strength of the sectors within the domain and (2) the number of sectors that are superimposed within an emission domain of interest. The two highest contributing sectors (On-road and Industry) received the most optimization from the inversion scheme, with the on-road sector tracking the daily proxy data closely. Additionally, one of the minor emission sectors (Marine) was responsive to the inversion scheme due to its predominance along the shore. Any heightened XCO_2 enhancements allocated to this region by X-STILT would be allocated to emissions from the commercial maritime sector.

Previous space-based instruments such as OCO-2 collect soundings in narrow transects during orbit that, when coincident with an urban CO_2 plume, can be used to calculate an enhancement (Wu et al., 2018; Yang et al., 2020). The broad coverage by OCO-3's SAM observations (roughly 80km × 80km) over urban areas reduces the amount of atmospheric mixing that occurs during transport between the source and observation points (soundings), allowing intra-city features to be resolved, thus improving the inversion's ability to optimize specific sectors. Furthermore, OCO-3's ability to collect SAMs at varying times of the day assists in disaggregating sectors with strong diurnal trends.

The results of this work highlight the potential of space-based observations to resolve sector-specific trends in carbon emissions within cities. Developing a global operational framework capable of assimilating data from current and future satellites has the potential to update worldwide emission inventories in near-real-time. Optimized high-resolution emission inventories can potentially reflect the effectiveness of carbon reduction policies at sub-annual time scales. However, shortcomings must be addressed. It is unclear as to how effective this inversion scheme will be when smaller cities are considered. Additionally, potential issues arise when point and area sources are mixed. Posterior scaling factors derived from a collection of independently varying point sources may not accurately scale emissions for all of the considered sources. Therefore, future work should address this shortcoming by assigning each point source a dedicated scaling factor in $\vec{\lambda}$. Obtaining high-resolution proxy data for the industry and/or power generation sectors could provide further insights into the dynamics exhibited by the optimized scaling factors.

4 Conclusions

As the level of atmospheric CO_2 increases, the implementation of local-to-international carbon reduction policies becomes more urgent. Monitoring and reporting emissions from urban areas is difficult with in-situ networks due to their high cost and maintenance, making global coverage unfeasible. Conversely, "bottom-up" accounting approaches (emission inventories) have the potential to provide global estimates of CO_2 emissions but these products can have large uncertainties and often lag several years behind. To remedy these shortcomings, space-based CO_2 observing systems provide near-global coverage of urban areas around the globe. The results of this work demonstrated that observations from such instruments have the potential to optimize sector-specific flux estimates provided by the Vulcan 3.0 emission inventory. In a Bayesian inversion scheme, sectors making up large fractions of the total emissions from the Los Angeles Basin were optimized and posterior values were compared with proxy data. Notably, the strongest two sectors in the basin (on-road transportation and industry) exhibited the most sensitivity to the optimization process. One of the smaller sectors (commercial maritime) also exhibited strong sensitivity. This was due to the lack of coincident sectors. Although several sectors were

optimized and correlated with proxy data, future work should move away from optimizing sectoral scaling factors and expand the inversion scheme to generate posterior percell corrections.

Open Research

All data used to support the conclusions of this work are open source. The locations of all proxy datasets are included in **Table 2.2.3**. The Vulcan 3.0 emission inventory is described by Gurney et al. (2020) and is freely available at https://daac.ornl.gov/cgi-bin/dsviewer.pl?ds_id=1741. SMUrF data is described in Wu et al. (2021) and can be found at https://daac.ornl.gov/NACP/guides/Biogenic_CO2flux_SIF_SMUrF.html. The X-STILT model used in this work (freely available) is described in Wu et al. (2018) and was driven by the High Resolution Rapid Refresh (HRRR) meteorology data provided by the Air Resources Laboratory (https://www.ready.noaa.gov/READYmetdata.php). Data from the OCO-3 instrument can be downloaded from NASA's GES DISC repository (https://disc.gsfc.nasa.gov/datasets/OCO3_L2_Lite_FP_10.4r/summary) after registering for a (free) account. All maps were generated using the ggmap package (Kahle & Wickham, 2013).

References

Bares, R., Mitchell, L., Fasoli, B., Bowling, D. R., Catharine, D., Garcia, M., ... Lin, J. C. (2019, August). The utah urban carbon dioxide (UUCON) and uintah basin greenhouse gas networks: instrumentation, data, and measurement uncertainty. *Earth System Science Data*, *11*(3), 1291–1308. Retrieved from https://doi.org/10.5194/essd-11-1291-2019 doi: 10.5194/essd-11-1291-2019

Benjamin, S. G., Weygandt, S. S., Brown, J. M., Hu, M., Alexander, C. R., Smirnova, T. G., ... Manikin, G. S. (2016, April). A north american hourly assimilation and model forecast cycle: The rapid refresh. *Monthly Weather Review*, *144*(4), 1669–1694. Retrieved from https://doi.org/10.1175/mwr-d-15-0242.1 doi: 10.1175/mwr-d-15-0242.1

Carter, C. A., Steinbach, S., & Zhuang, X. (2022, July). Supply chain disruptions and containerized agricultural exports from california ports. *Applied Economic Perspectives and Policy*. Retrieved from https://doi.org/10.1002/aepp.13311 doi: 10.1002/aepp.13311

Crisp, D., Atlas, R., Breon, F.-M., Brown, L., Burrows, J., Ciais, P., ... Schroll, S. (2004, January). The orbiting carbon observatory (OCO) mission. *Advances in Space Research*, *34*(4), 700–709. Retrieved from https://doi.org/10.1016/j.asr.2003.08.062 doi: 10.1016/j.asr.2003.08.062

Eldering, A., Taylor, T. E., O'Dell, C. W., & Pavlick, R. (2019, April). The OCO-3 mission: measurement objectives and expected performance based on 1 year of simulated data. *Atmospheric Measurement Techniques*, *12*(4), 2341–2370. Retrieved from https://doi.org/10.5194/amt-12-2341-2019 doi: 10.5194/amt-12-2341-2019

EPA. (2021, November). *The 2021 automotive trends report* (Tech. Rep. No. EPA-420-R-21-023). United States' Environmental Protection Agency.

Gilfillan, D., & Marland, G. (2021, April). CDIAC-FF: global and national CO_2 emissions from fossil fuel combustion and cement manufacture: 1751–2017. *Earth System Science Data*, *13*(4), 1667–1680. Retrieved from `https://doi.org/10.5194/essd-13-1667-2021` doi: 10.5194/essd-13-1667-2021

Gurney, K. R., Liang, J., Patarasuk, R., Song, Y., Huang, J., & Roest, G. (2020, October). The vulcan version 3.0 high-resolution fossil fuel CO_2 emissions for the united states. *Journal of Geophysical Research: Atmospheres*, *125*(19). Retrieved from `https://doi.org/10.1029/2020jd032974` doi: 10.1029/2020jd032974

Hakkarainen, J., Ialongo, I., & Tamminen, J. (2016, November). Direct space-based observations of anthropogenic CO_2 emission areas from OCO-2. *Geophysical Research Letters*, *43*(21). Retrieved from `https://doi.org/10.1002/2016gl070885` doi: 10.1002/2016gl070885

Hedelius, J. K., Liu, J., Oda, T., Maksyutov, S., Roehl, C. M., Iraci, L. T., ... Wennberg, P. O. (2018, November). Southern california megacity CO_2, CH_4, and CO flux estimates using ground- and space-based remote sensing and a lagrangian model. *Atmospheric Chemistry and Physics*, *18*(22), 16271–16291. Retrieved from `https://doi.org/10.5194/acp-18-16271-2018` doi: 10.5194/acp-18-16271-2018

Huang, L., Tan, Y., & Guan, X. (2022, June). Hub-and-spoke network design for container shipping considering disruption and congestion in the post COVID-19 era. *Ocean & Coastal Management*, *225*, 106230. Retrieved from `https://doi.org/10.1016/j.ocecoaman.2022.106230` doi: 10.1016/j.ocecoaman.2022.106230

Hutchins, M. G., Colby, J. D., Marland, G., & Marland, E. (2016, March). A comparison of five high-resolution spatially-explicit, fossil-fuel, carbon dioxide emission inventories for the united states. *Mitigation and Adaptation Strategies for Global Change*, *22*(6), 947–972. Retrieved from `https://doi.org/10.1007/s11027-016-9709-9` doi: 10.1007/s11027-016-9709-9

Intergovernmental Panel on Climate Change. (2015). *Climate change 2014: Mitigation of climate change*. Cambridge, England: Cambridge University Press.

Janssens-Maenhout, G., Crippa, M., Guizzardi, D., Muntean, M., Schaaf, E., Dentener, F., ... Oreggioni, G. D. (2019, July). EDGAR v4.3.2 global atlas of the three major greenhouse gas emissions for the period 1970–2012. *Earth System Science Data*, *11*(3), 959–1002. Retrieved from `https://doi.org/10.5194/essd-11-959-2019` doi: 10.5194/essd-11-959-2019

Janssens-Maenhout, G., Pinty, B., Dowell, M., Zunker, H., Andersson, E., Balsamo, G., ... Veefkind, P. (2020, August). Toward an operational anthropogenic CO2 emissions monitoring and verification support capacity. *Bulletin of the American Meteorological Society*, *101*(8), E1439–E1451. Retrieved from `https://doi.org/10.1175/bams-d-19-0017.1` doi: 10.1175/bams-d-19-0017.1

Kahle, D., & Wickham, H. (2013). ggmap: Spatial visualization with ggplot2. *The R Journal*, *5*(1), 144–161. Retrieved from `https://journal.r-project.org/archive/2013-1/kahle-wickham.pdf`

Keppel-Aleks, G., Wennberg, P. O., & Schneider, T. (2011, April). Sources of variations in total column carbon dioxide. *Atmospheric Chemistry and Physics*, *11*(8), 3581–3593. Retrieved from `https://doi.org/10.5194/acp-11-3581-2011` doi: 10.5194/acp-11-3581-2011

Kiel, M., Eldering, A., Roten, D. D., Lin, J. C., Feng, S., Lei, R., ... Iraci, L. T. (2021, June). Urban-focused satellite CO_2 observations from the orbiting carbon observatory-3: A first look at the los angeles megacity. *Remote Sensing of Environment*, *258*, 112314. Retrieved from `https://doi.org/10.1016/j.rse.2021.112314` doi: 10.1016/j.rse.2021.112314

Kunik, L., Mallia, D. V., Gurney, K. R., Mendoza, D. L., Oda, T., & Lin, J. C.

(2019, January). Bayesian inverse estimation of urban CO_2 emissions: Results from a synthetic data simulation over salt lake city, UT. *Elementa: Science of the Anthropocene*, *7*. Retrieved from `https://doi.org/10.1525/elementa.375` doi: 10.1525/elementa.375

Laughner, J. L., Neu, J. L., Schimel, D., Wennberg, P. O., Barsanti, K., Bowman, K. W., ... and, Z.-C. Z. (2021, November). Societal shifts due to COVID-19 reveal large-scale complexities and feedbacks between atmospheric chemistry and climate change. *Proceedings of the National Academy of Sciences*, *118*(46). Retrieved from `https://doi.org/10.1073/pnas.2109481118` doi: 10.1073/pnas.2109481118

Lauvaux, T., Gurney, K. R., Miles, N. L., Davis, K. J., Richardson, S. J., Deng, A., ... Turnbull, J. (2020, August). Policy-relevant assessment of urban CO_2 emissions. *Environmental Science & Technology*, *54*(16), 10237–10245. Retrieved from `https://doi.org/10.1021/acs.est.0c00343` doi: 10.1021/acs.est.0c00343

Lauvaux, T., Miles, N. L., Deng, A., Richardson, S. J., Cambaliza, M. O., Davis, K. J., ... Wu, K. (2016, May). High-resolution atmospheric inversion of urban CO_2 emissions during the dormant season of the indianapolis flux experiment (INFLUX). *Journal of Geophysical Research: Atmospheres*, *121*(10), 5213–5236. Retrieved from `https://doi.org/10.1002/2015jd024473` doi: 10.1002/2015jd024473

Lu, S., Wang, J., Wang, Y., & Yan, J. (2018, March). Analysis on the variations of atmospheric CO_2 concentrations along the urban–rural gradients of chinese cities based on the OCO-2 XCO data. *International Journal of Remote Sensing*, *39*(12), 4194–4213. Retrieved from `https://doi.org/10.1080/01431161.2017.1415482` doi: 10.1080/01431161.2017.1415482

Mallia, D. V., Mitchell, L. E., Kunik, L., Fasoli, B., Bares, R., Gurney, K. R., ... Lin, J. C. (2020, December). Constraining urban CO_2 emissions using mobile observations from a light rail public transit platform. *Environmental Science & Technology*, *54*(24), 15613–15621. Retrieved from `https://doi.org/10.1021/acs.est.0c04388` doi: 10.1021/acs.est.0c04388

Miller, J. B., Lehman, S. J., Verhulst, K. R., Miller, C. E., Duren, R. M., Yadav, V., ... Sloop, C. D. (2020, October). Large and seasonally varying biospheric CO_2 fluxes in the los angeles megacity revealed by atmospheric radiocarbon. *Proceedings of the National Academy of Sciences*, *117*(43), 26681–26687. Retrieved from `https://doi.org/10.1073/pnas.2005253117` doi: 10.1073/pnas.2005253117

Oda, T., Maksyutov, S., & Andres, R. J. (2018, January). The open-source data inventory for anthropogenic CO_2, version 2016 (ODIAC2016): a global monthly fossil fuel CO_2 gridded emissions data product for tracer transport simulations and surface flux inversions. *Earth System Science Data*, *10*(1), 87–107. Retrieved from `https://doi.org/10.5194/essd-10-87-2018` doi: 10.5194/essd-10-87-2018

Rayner, P. J., & O'Brien, D. M. (2001, January). The utility of remotely sensed CO_2 concentration data in surface source inversions. *Geophysical Research Letters*, *28*(1), 175–178. Retrieved from `https://doi.org/10.1029/2000gl011912` doi: 10.1029/2000gl011912

Rodgers, C. D. (2000). *Inverse methods for atmospheric sounding*. WORLD SCIENTIFIC. Retrieved from `https://doi.org/10.1142/3171` doi: 10.1142/3171

Roten, D., Lin, J. C., Kunik, L., Mallia, D., Wu, D., Oda, T., & Kort, E. A. (2022, May). The information content of dense carbon dioxide measurements from space: A high-resolution inversion approach with synthetic data from the OCO-3 instrument. *Atmospheric Chemistry and Physics*. Retrieved from `https://doi.org/10.5194/acp-2022-315` doi: 10.5194/acp-2022-315

Roten, D., Marland, G., Bun, R., Crippa, M., Gilfillan, D., Jones, M., ... Andrew,

R. (2022, March 14). Co2 emissions from energy systems and industrial processes: Inventories from data- and proxy-driven approaches. In *Balancing greenhouse gas budgets* (1st ed.). Netherlands: Elsevier.

Shekhar, A., Chen, J., Paetzold, J. C., Dietrich, F., Zhao, X., Bhattacharjee, S., . . . Wofsy, S. C. (2020, September). Anthropogenic CO_2 emissions assessment of nile delta using XCO_2 and SIF data from OCO-2 satellite. *Environmental Research Letters*, *15*(9), 095010. Retrieved from `https://doi.org/10.1088/1748-9326/ab9cfe` doi: 10.1088/1748-9326/ab9cfe

Shusterman, A. A., Teige, V. E., Turner, A. J., Newman, C., Kim, J., & Cohen, R. C. (2016, October). The BErkeley atmospheric CO_2 observation network: initial evaluation. *Atmospheric Chemistry and Physics*, *16*(21), 13449–13463. Retrieved from `https://doi.org/10.5194/acp-16-13449-2016` doi: 10.5194/acp-16-13449-2016

Taylor, T. E., Eldering, A., Merrelli, A., Kiel, M., Somkuti, P., Cheng, C., . . . Yu, S. (2020, December). OCO-3 early mission operations and initial (vEarly) XCO_2 and SIF retrievals. *Remote Sensing of Environment*, *251*, 112032. Retrieved from `https://doi.org/10.1016/j.rse.2020.112032` doi: 10.1016/j.rse.2020.112032

Turner, A. J., Kim, J., Fitzmaurice, H., Newman, C., Worthington, K., Chan, K., . . . Cohen, R. C. (2020, November). Observed impacts of COVID-19 on urban CO_2 emissions. *Geophysical Research Letters*, *47*(22). Retrieved from `https://doi.org/10.1029/2020gl090037` doi: 10.1029/2020gl090037

Wu, D., Lin, J. C., Duarte, H. F., Yadav, V., Parazoo, N. C., Oda, T., & Kort, E. A. (2021, June). A model for urban biogenic CO_2 fluxes: Solar-induced fluorescence for modeling urban biogenic fluxes (SMUrF v1). *Geoscientific Model Development*, *14*(6), 3633–3661. Retrieved from `https://doi.org/10.5194/gmd-14-3633-2021` doi: 10.5194/gmd-14-3633-2021

Wu, D., Lin, J. C., Fasoli, B., Oda, T., Ye, X., Lauvaux, T., . . . Kort, E. A. (2018, December). A lagrangian approach towards extracting signals of urban CO_2 emissions from satellite observations of atmospheric column CO_2 (XCO_2): X-stochastic time-inverted lagrangian transport model ("x-STILT v1"). *Geoscientific Model Development*, *11*(12), 4843–4871. Retrieved from `https://doi.org/10.5194/gmd-11-4843-2018` doi: 10.5194/gmd-11-4843-2018

Wu, D., Lin, J. C., Oda, T., & Kort, E. A. (2020, February). Space-based quantification of per capita CO_2 emissions from cities. *Environmental Research Letters*, *15*(3), 035004. Retrieved from `https://doi.org/10.1088/1748-9326/ab68eb` doi: 10.1088/1748-9326/ab68eb

Yang, E. G., Kort, E. A., Wu, D., Lin, J. C., Oda, T., Ye, X., & Lauvaux, T. (2020, April). Using space-based observations and lagrangian modeling to evaluate urban carbon dioxide emissions in the middle east. *Journal of Geophysical Research: Atmospheres*, *125*(7). Retrieved from `https://doi.org/10.1029/2019jd031922` doi: 10.1029/2019jd031922

Ye, X., Lauvaux, T., Kort, E. A., Oda, T., Feng, S., Lin, J. C., . . . Wu, D. (2020, April). Constraining fossil fuel CO_2 emissions from urban area using OCO-2 observations of total column CO_2. *Journal of Geophysical Research: Atmospheres*, *125*(8). Retrieved from `https://doi.org/10.1029/2019jd030528` doi: 10.1029/2019jd030528

Zhong, W., & Haigh, J. D. (2013, March). The greenhouse effect and carbon dioxide. *Weather*, *68*(4), 100–105. Retrieved from `https://doi.org/10.1002/wea.2072` doi: 10.1002/wea.2072